ISSN 2072-5981
doi: 10.26907/mrsej

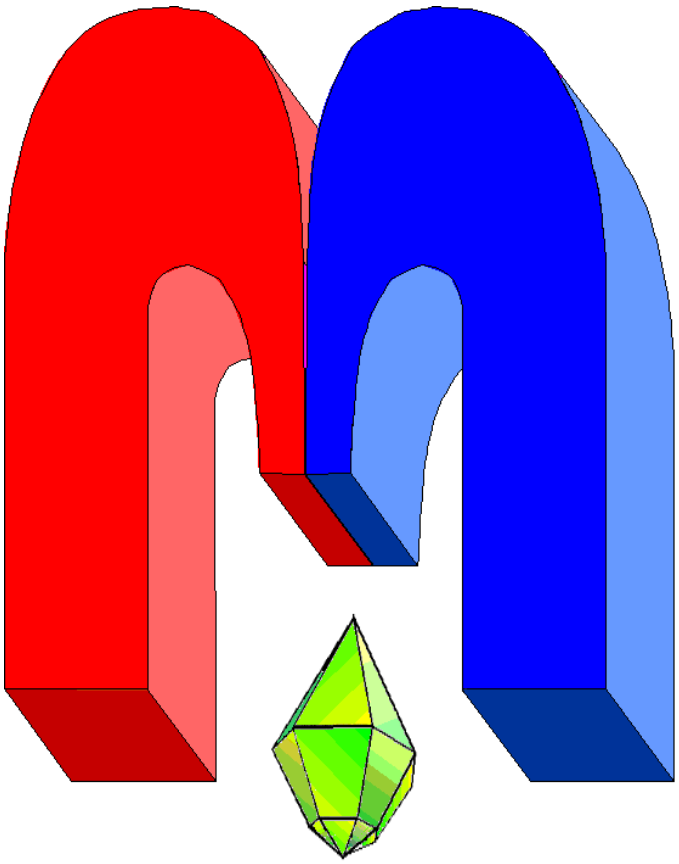

Magnetic Resonance in Solids

Electronic Journal

Volume ***28***
Issue ***2***
Article No ***26202***
1-22 pages
2026
doi: **10.26907/mrsej-26202**

http://mrsej.ru
(http://mrsej. kpfu.ru)

Established and published by Kazan University*
Endorsed by International Society of Magnetic Resonance (ISMAR)
Registered by Russian Federation Committee on Press (#015140), August 2, 1996
First Issue appeared on July 25, 1997

"***Magnetic Resonance in Solids. Electronic Journal***" (**MRS*ej***) is a peer-reviewed, all electronic journal, publishing articles which meet the highest standards of scientific quality in the field of basic research of a magnetic resonance in solids and related phenomena.

Indexed and abstracted by
Web of Science (ESCI, Clarivate Analytics, from 2015),White List (from 2023) *Scopus* (Elsevier, from 2012), *RusIndexSC* (*eLibrary*, from 2006), *Google Scholar*, *DOAJ*, *ROAD*, *CyberLeninka* (from 2006), *SCImago Journal & Country Rank*, etc.

* Address: "Magnetic Resonance in Solids. Electronic Journal", Kazan Federal University; Kremlevskaya str., 18; Kazan 420008, Russia

† In Kazan University the Electron Paramagnetic Resonance (EPR) was discovered by Zavoisky E.K. in 1944.

Electron Spin Echo Envelope Modulation of Spin-Polarized Photoexcited Triplet States: Application to $Y_3N@C_{80}$

Yu.E. Kandrashkin*, R.B. Zaripov**

Zavoisky Physical-Technical Institute, FRC Kazan Scientific Center of RAS, Kazan 420029, Russia

**E-mail: yuk@kfti.knc.ru*

***E-mail: rb.zaripov@knc.ru*

(received April 28, 2026; revised August 24, 2026; accepted August 28, 2026; published September 1, 2026)

Electron spin echo envelope modulation (ESEEM) spectroscopy provides detailed information on electron-nuclear hyperfine interactions and has also been successfully applied to photoexcited triplet states. However, the interpretation of two-dimensional (2D) field-swept ESEEM patterns in disordered triplet systems remains challenging. In this study, we provide analytical and numerical descriptions of ESEEM in photoexcited triplet states ($S = 1$) within the high-field regime. We derive analytical expressions for the nuclear modulation frequencies and depths associated with individual electron paramagnetic resonance (EPR) transitions at specific resonance positions where the external magnetic field aligns with the principal axes of the ZFS tensor. At these positions, the ESEEM response simplifies and exhibits characteristic differences between the two allowed EPR transition branches, providing direct access to the sign of the ZFS parameter D and to the orientation of the hyperfine coupling tensor. Numerical simulations of 2D ESEEM spectra confirm the analytical predictions and demonstrate pronounced intensity asymmetries that depend on these parameters. The developed approach is applied to the analysis of 2D ESEEM experimental data for the photoexcited triplet state of the endohedral fullerene $Y_3N@C_{80}$, providing a consistent interpretation of hyperfine interactions involving both ^{89}Y and ^{13}C nuclei. The results establish 2D ESEEM as a powerful method for the characterization of photoexcited triplet states in polycrystalline samples.

PACS: 76.70.Dx, 29.30.-h, 07.50.-e

Keywords: electron paramagnetic resonance, electron spin echo envelope modulation, endohedral fullerene, laser excitation, dipolar coupling, hyperfine interaction

1. Introduction

Photoexcited states of organic molecules play a central role in a wide range of scientific and technological applications [1–3], including solar energy conversion [4], photodynamic therapy [5], molecular electronics, and quantum information science [6, 7]. The performance of such molecular systems critically depends on the formation and subsequent evolution of metastable states with nonzero spin ($S \neq 0$). Time-resolved electron paramagnetic resonance (TREPR) spectroscopy is a well-established method for characterizing the spectral and kinetic properties of these states [8, 9]. Furthermore, the strong non-equilibrium spin polarization often accompanying photoexcited metastable states, arising from spin-selective intra- and intermolecular electron transition processes, enables the detection of weak hyperfine interactions (HFIs) using transient magnetic resonance techniques such as electron–nuclear double resonance (ENDOR) and electron spin echo envelope modulation (ESEEM) spectroscopy [10–13].

ESEEM spectroscopy is a well-established pulsed EPR method for probing hyperfine couplings between electron spin and nearby nuclear spins. The theoretical description of ESEEM in $S = 1/2$ systems is well developed [14–19]. In photoexcited spin-polarized triplet ($S = 1$) states, ESEEM has been addressed in a number of earlier studies and has already demonstrated its potential for extracting structural and dynamical information [12, 20–24]. In particular, the

early room-temperature studies of pentacene and anthracene established the feasibility of triplet ESEEM measurements, developed the high-field treatment for $S = 1$ systems, and demonstrated the extraction of ENDOR-like frequencies and hyperfine tensor information [22, 23]. These developments were subsequently summarized in Lin's review of ESE spectroscopy of organic triplets [24]. A major challenge in triplet systems is the presence of zero-field splitting (ZFS), which introduces a strong orientation dependence in both resonance conditions and spin polarization, especially in disordered or polycrystalline samples.

The ZFS of the triplet spin causes the EPR transition frequencies to depend sensitively on the orientation of the molecule with respect to the external magnetic field [13, 25–27]. In addition, the spin-selective processes inducing the non-equilibrium spin polarization of the metastable triplet state of the chromophore are predominantly determined by intramolecular processes and are therefore essentially anisotropic. While these effects complicate the interpretation of TREPR and ESEEM spectra, they also provide valuable information by linking HFI to the molecular frame defined by the principal axes of the ZFS tensor. Consequently, characteristic features in ENDOR and ESEEM spectra may, in principle, be correlated with the spatial position of nuclei relative to the molecular frame. However, the analysis of field-dependent 2D ESEEM patterns in disordered triplet systems remains insufficiently systematized, particularly with respect to the relation between modulation asymmetries, the sign of D, and the orientation of the principal axes of the HFI tensor in the molecular frame.

In this work, we present an analytical and numerical treatment of 2D field-swept ESEEM for spin-polarized triplet states in the high-field limit. We derive analytical expressions for the nuclear modulation frequencies and depths associated with individual EPR transitions. We demonstrate that significant simplifications occur at particular resonance positions that correspond to molecular orientations where the external magnetic field aligns with the principal axes of the ZFS tensor. At these magnetic field positions, referred to here as turning points, the ESEEM response exhibits features that directly reflect the sign of the ZFS parameter D and the dipole coupling axis. We validate the analytical results by simulating 2D field-swept ESEEM spectra numerically and applying them to experimental data obtained for the photoexcited triplet state of the endohedral fullerene $Y_3N@C_{80}$. The results show that 2D ESEEM provides information complementary to TREPR and enables the extraction of hyperfine and ZFS-related parameters that are not readily accessible by TREPR spectroscopy alone.

2. Model

2.1. Spectral Properties

Upon photoexcitation, the chromophore forms a triplet excited state with total spin $S = 1$. The corresponding spin Hamiltonian contains two main terms:

$$H_{\mathrm{T}} = H_{\mathrm{Z}} + H_{\mathrm{ZFS}}. \tag{1}$$

The Zeeman interaction of the chromophore,

$$H_{\mathrm{Z}} = g\beta_{\mathrm{e}} B S_z = \hbar\omega_{\mathrm{T}} S_z, \tag{2}$$

is determined by the angular frequency, $\omega_{\mathrm{T}} = g\beta_{\mathrm{e}} B\hbar^{-1}$, assuming the electron g-factor is isotropic, which is a good approximation for metal-free organic molecules. The other symbols have their usual meanings in magnetic resonance.

The ZFS is given by

$$H_{\mathrm{ZFS}}/\hbar = D(S_Z^2 - \mathbf{S}^2/3) + E(S_X^2 - S_Y^2). \tag{3}$$

The spin operator of the triplet state S_z (eq. (2)) is defined in the laboratory frame. Hereafter, the letters $\xi = x, y, z$ denote the laboratory frame axes. The operators $S_{\xi=X,Y,Z}$ (eq. (3)) are defined in the molecular frame (along the principal axes $\xi = X, Y, Z$ of the ZFS tensor). The parameters D and E describe the axial and rhombic characters of the ZFS, respectively.

We consider the high-field approximation, in which the ZFS is significantly smaller than the Zeeman energy:

$$|D|, |E| \ll \omega_{\mathrm{T}}. \tag{4}$$

The molecule in the triplet state has two EPR transitions $\psi_{+1} \leftrightarrow \psi_0$ and $\psi_{-1} \leftrightarrow \psi_0$ with $|\Delta m| = 1$ between the eigenstates ψ_m of the Hamiltonian (1) corresponding to the magnetic quantum number of the electron spin $m = 0, \pm 1$. The corresponding resonance conditions of the EPR transitions are:

$$\begin{aligned} \Delta E_+ &= E_+ - E_0 = \omega_{\mathrm{MW}}, \\ \Delta E_- &= E_0 - E_- = \omega_{\mathrm{MW}}. \end{aligned} \tag{5}$$

Here, ω_{MW} is the microwave (MW) frequency, and $E_{m=0,\pm1} = \langle H_{\mathrm{T}} \rangle_m$ is the energy of the eigenstate ψ_m. Hereafter, the expectation value of an operator O is defined as $\langle O \rangle_m \equiv \langle \psi_m | O | \psi_m \rangle$. For the sake of simplicity, whenever it is ambiguous, the indices of the parameters relating to $m = \pm 1$ are denoted as $\pm$.

The initial populations of the metastable triplet state are determined by the intersystem crossing (ISC) pathways from the photoexcited singlet state. ISC requires a change in spin multiplicity, making this process spin-selective. In typical chromophores, the ISC is governed by the spin orbit coupling (SOC) and doesn't depend on the external fields. As a result, the initial polarization has a multiplet character and is determined by the populations of the states of the molecular frame. Therefore, the density matrix can be expressed via the populations $p_{X,Y,Z}$ of the corresponding states as follows:

$$\rho = p_X(1 - S_X^2) + p_Y(1 - S_Y^2) + p_Z(1 - S_Z^2). \tag{6}$$

The intensity of the EPR signal is proportional to the difference in populations between the states:

$$\Delta p_{\pm} \equiv \Delta p_{\pm 1,0} = \mp\big(\langle \rho \rangle_{\pm 1} - \langle \rho \rangle_0\big). \tag{7}$$

The above expressions show that the initial triplet state is formed in the molecular frame (6), while EPR spectrum is recorded under conditions in which the Zeeman interaction dominates (4). Consequently, the EPR signal intensity depends on the orientation of the molecule relative to the laboratory frame. Furthermore, the resonance field, B_{res}, determined by equations (5) also depends on the orientation of the molecule. As a result, in a polycrystalline sample, the intensity of the EPR line depends on the relative number of the photoexcited chromophores, $f_{ij} = f(\psi_i \leftrightarrow \psi_j)$, those are in resonance (5) at a particular value of the magnetic field $B = B_{\mathrm{res}}$ and the spin polarization (7) at the given conditions. Both these factors depend on the molecular orientation in respect to the laboratory frame. Therefore, the EPR signal at $B = B_{\mathrm{res}}$ can be obtained by the following expression:

$$I_{\mathrm{EPR}}(B = B_{\mathrm{res}}) = \sum_{i \neq j} \int f_{ij}(B)\, \Delta p_{ij}(B)\, \sin\theta \, d\theta \, d\varphi. \tag{8}$$

Here θ and φ are the polar and azimuthal angles defining the direction of the external magnetic field in the frame of the ZFS tensor.

In high field limit, the resonance transitions $\psi_{+1} \leftrightarrow \psi_0$ and $\psi_{-1} \leftrightarrow \psi_0$ according to (5) occur at

$$B_{\rm res} = B_0 \pm \Delta B. \tag{9}$$

Here, ΔB is the shift of the magnetic field relative to the central point B_0 where the energy gaps $\Delta E_\pm$ become equal:

$$B_0 = \hbar\omega_{\rm MW}/g\beta_{\rm e}. \tag{10}$$

As a consequence, the probability function of the two transition branches is symmetric relative to the central point $f_{0,+1}(B_0 + \Delta B) = f_{0,-1}(B_0 - \Delta B)$. The multiplet character of the spin polarization in high-field limit provides equal populations of the states $\psi_\pm$, $\langle\rho\rangle_{+1} = \langle\rho\rangle_{-1}$, and therefore $\Delta p_+ = -\Delta p_-$ (see eq. (7)). Thus, the EPR spectrum has equal intensity of the absorptive and emissive parts. As a result, the properties of the time resolved EPR (TREPR) spectrum are antisymmetric relative to the central point $I_{\rm EPR}(B_0 + \Delta B) = -I_{\rm EPR}(B_0 - \Delta B)$.

The main properties of the EPR signal and nuclear spin coherences, induced by a transition initiated by a microwave field, are presented in Fig. 1. The energy levels of the triplet state are presented for two orientations of the magnetic field with respect to the molecular frame: $\mathbf{B} \parallel \mathbf{Z}$ and $\mathbf{B} \parallel \mathbf{X}$. The stick spectra are shown for the given density matrix $\rho \sim |T_Z\rangle\langle T_Z| = (1 - S_Z^2)$ (see (6)), the non-equilibrium populations distributed over the energy levels in the zero field and in the high field limit (typical for the EPR experiment) are shown by small disks. Note, that the stick spectrum is given for orientations $\mathbf{B} \parallel \mathbf{X}$, $\mathbf{B} \parallel \mathbf{Y}$, $\mathbf{B} \parallel \mathbf{Z}$. In polycrystalline samples, the relative intensities of the EPR signal are determined by spin polarization and the relative fraction of the molecules those are in the resonance conditions (function f).

The following parameters are presented with references to the corresponding equations defined below (the remaining parameters are determined analogously): the central point B_0 (10); the turning points $B_{\xi=X,Y,Z}$ (24), determined by the magnetic field offsets $\Delta B_{\xi=X,Y,Z}$ (25); and the effective nuclear magnetic fields $\mathbf{B}^{\rm eff}_{m=0,\pm1}$, which include both the Zeeman ($\mathbf{B}$) and hyperfine ($\mathbf{B}_{\rm HFI}$) contributions. The splittings between the nuclear spin sublevels are proportional to the modulation frequencies $\Omega_{m=0,\pm1} \sim |\mathbf{B}^{\rm eff}_m|$ (eq. (18), not shown). The EPR transition produces coherence between nuclear spin sublevels. This coherence is governed by the degree of non-collinearity between the nuclear effective fields of the initial and final states $|\mathbf{B}^{\rm eff}_{\pm0} \times \mathbf{B}^{\rm eff}_{\pm1}|^2$ (see eq. (19)). The signs here correspond to the EPR transition branches (see eq. (5)).

2.2. Nuclear Effective Field

The interaction with nearby nuclei splits the electron's energy structure, including nuclear spin sublevels. The simplest case (electron spin $S = 1$ and nuclear spin $I = 1/2$) is shown in Fig. 1. The magnetic nucleus ($I = 1/2$) experiences the Zeeman interaction with the external magnetic field and HFI. The former is determined by the angular frequency $\omega_{\rm n}$, while the latter is determined by the tensor T:

$$H_{\rm n} = H_{\rm nZ} + H_{\rm HFI}, \tag{11}$$

$$H_{\rm nZ}/\hbar = -\gamma_{\rm n} B I_z = -\omega_{\rm n} I_z, \tag{12}$$

$$H_{\rm HFI}/\hbar = \mathbf{S} \cdot T \cdot \mathbf{I} = \omega_{\rm iso}\, \mathbf{S} \cdot \mathbf{I} + \omega_{\rm dd}\big(3(\mathbf{S} \cdot \mathbf{r})(\mathbf{I} \cdot \mathbf{r}) - \mathbf{S} \cdot \mathbf{I}\big). \tag{13}$$

The HFI includes the Fermi contact and dipole-dipole interaction terms with their respective angular frequencies, $\omega_{\rm iso}$ and

$$\omega_{\rm dd} = (\mu_0/4\pi)(g\beta_{\rm e})(\gamma_{\rm n}\hbar)/r_0^3. \tag{14}$$

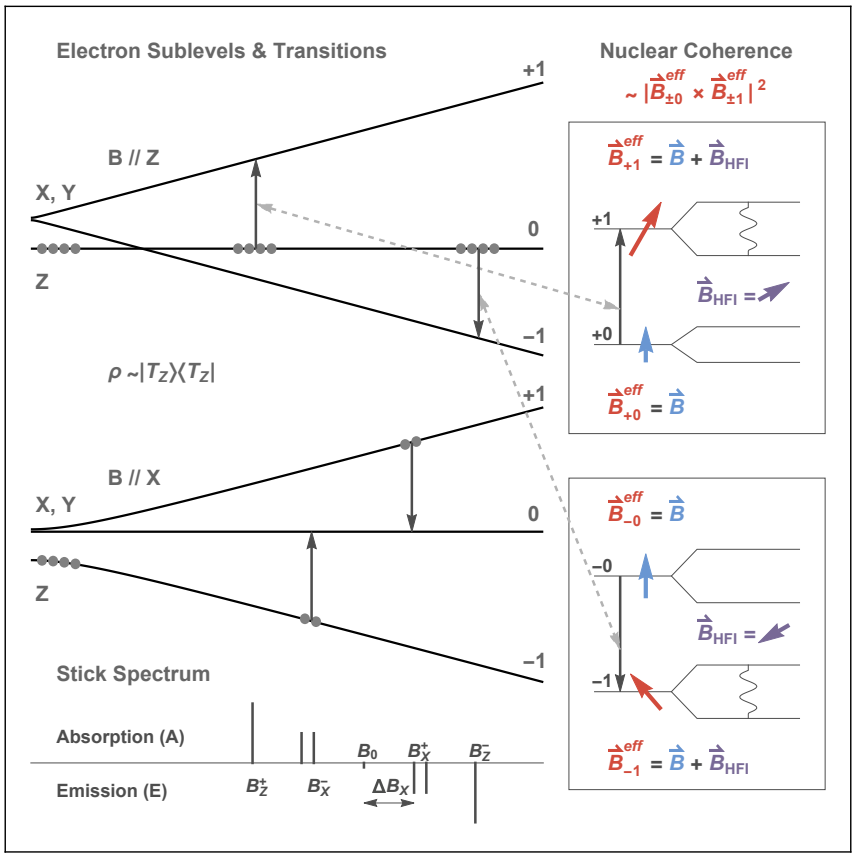

Figure 1. Schematic representation of the main processes involved in EPR transitions of a triplet state ($S = 1$) interacting with a single nucleus ($I = 1/2$) during an ESEEM experiment, with the key notations used throughout the text. The main panel shows the magnetic-field dependence of the spin sublevels for two orientations of the external field ($\mathbf{B} \parallel \mathbf{X}$ and $\mathbf{B} \parallel \mathbf{Z}$). Only the transitions at $B = B_Z$ and $B = B_X$ are shown. The stick spectrum at the bottom illustrates the spin polarization pattern arising from transitions along all three principal axes of the molecular frame.

The dipolar coupling depends on the unit vector $\mathbf{r}$, which defines the direction connecting the electron and the nucleus, and on the distance between two spins r_0. Typically, the nuclear spin interactions described by Hamiltonian (11) are much weaker than the leading interactions of the electron spin (1):

$$|\omega_{\mathrm{n}}|, |\omega_{\mathrm{iso}}|, |\omega_{\mathrm{dd}}| \ll |\omega_{\mathrm{T}}|. \tag{15}$$

As a result, the influence of the nuclear spin on the mixing of the electron spin wavefunctions $\psi_{m=0,\pm1}$ is negligible, and only the secular and pseudo-secular terms of the Hamiltonian (11) are relevant in ESEEM experiments. Consequently, the Hilbert space of the total spin system can be decomposed into subspaces corresponding to the eigenstates of the electron spin [28, 29]:

$$H_m \equiv \langle\psi_m|H|\psi_m\rangle = \hbar\left(-\omega_{\mathrm{n}} I_z + \sum_{\xi} \langle S_\xi\rangle_m T_{\xi\zeta} I_\zeta\right). \tag{16}$$

The action of the spin Hamiltonian (16) is convenient to describe in terms of the effective field $\mathbf{B}^{\mathrm{eff}}$, $H_m = -\hbar\gamma_{\mathrm{n}}\mathbf{B}_m \cdot \mathbf{I}$ [28, 30]. It consists of two contributions, including the Zeeman ($\mathbf{B}$) and hyperfine ($\mathbf{B}_{\mathrm{HFI}}$) interactions as shown in Fig. 1 and is determined by the components given in

the basis of the laboratory frame as:

$$\mathbf{B}_m = \mathbf{B} + \mathbf{B}_{\mathrm{HFI}} = \big(0, 0, B\big) - \gamma_{\mathrm{n}}^{-1} \sum_{\xi} \big(\langle S_\xi \rangle_m T_{\xi x},\ \langle S_\xi \rangle_m T_{\xi y},\ \langle S_\xi \rangle_m T_{\xi z}\big). \tag{17}$$

By definition, the effective field (17) depends on the projection m of the electron spin, and its direction varies with the m-value. Consequently, the nuclear spin wavefunctions are mixed by the EPR transition. As a result, the MW excitation not only forms the electron spin coherence but also induces the nuclear spin coherence (see Fig. 1). The latter is revealed as a modulation of the spin echo and can be studied using the ESEEM method.

2.3. ESEEM Formalism

The modulations of the spin echo envelope can be recorded by different EPR pulse techniques, including one- and two-dimensional methods such as ESEEM and HYSCORE sequences. Below we will describe the properties of ESEEM data obtained by primary and stimulated echo. The time dependence of the ESEEM signal $V(t)$ is well formulated [14–18]. This function can be expressed as a sum of trigonometric functions describing the evolution of nuclear spin coherences. For convenience, the basic expressions for $V(t)$ are summarized in Appendix A.

In general, interference of the spin evolution of nuclear coherences originating from several nearby nuclei complicates the interpretation of the ESEEM data. However, there are situations in which the description of the ESEEM signal is straightforward. This occurs when the coherence of a single nucleus dominates $k(\mathrm{nucleus}_i) \gg k(\mathrm{nucleus}_{j\neq i})$ or when the modulation depths are small ($k(\mathrm{nucleus}_i)k(\mathrm{nucleus}_j) \ll 1$). In the latter case, the function $V(t)$ reduces to a sum of single sinusoids determined by the modulation frequency (18) and the modulation depth k (19) of individual nuclei.

Additional complications arise from nonuniform phases accumulated during the interpulse intervals. For the given nuclei, this effect can be eliminated by an appropriate choice of the interpulse delay [31]. Another difficulty is the appearance of combination peaks, which occurs in the case of the primary echo sequence (see Appendix A). A detailed analysis of these effects is beyond the scope of the present work. Instead, our focus is on the analysis of Fourier-transformed data as a function of the resonance conditions of the triplet state. Within this approach, we analyze the contribution of a single nucleus to the Fourier spectrum, assuming that the contributions of individual nuclei are additive, as discussed above. In the following, we consider a triplet state interacting with a single nucleus whose contribution to the ESEEM signal is dominant.

In ESEEM experiment, excitation of the transition $\psi_i \leftrightarrow \psi_j$ produces nuclear spin coherence of both involved electron spin states. For a given state m, the oscillation frequency of the nuclear coherence is given by the energy splitting between the corresponding spin sublevels and is expressed by the magnitude of the effective field ($B_m^{\mathrm{eff}} = |\mathbf{B}_m^{\mathrm{eff}}|$) as follows:

$$\Omega_m = \gamma_{\mathrm{n}} B_m^{\mathrm{eff}} / \hbar. \tag{18}$$

The amplitude of nuclear coherence is determined by the degree of noncollinearity of effective fields. When an EPR transition is excited between electron states $m = i$ and $m = j$, the amplitude of the nuclear spin oscillation is equal to:

$$k_{ij} = 1 - (\mathbf{n}_i \cdot \mathbf{n}_j)^2. \tag{19}$$

Here, the quantization axis $\mathbf{n}_m$ is defined by the unit vector along the effective field (17):

$$\mathbf{n}_m = \mathbf{B}_m^{\text{eff}} / B_m^{\text{eff}}. \tag{20}$$

Within this approximation the intensity of the ESEEM Fourier transform peak is proportional to the modulation depth k (19).

As discussed above, the intensity of the EPR signal in a polycrystalline sample depends on the probability of molecules having resonance conditions f and electron spin polarization Δp (9). Similarly, the ESEEM peak, induced by the EPR transition $\psi_i \leftrightarrow \psi_j$ and corresponding to the modulation frequency $\Omega_{m=0,\pm1}$, equals:

$$I_{\text{ESEEM}}(B, \Omega) = \sum_{i \neq j} \Delta p_{ij}(B)\, f_{ij}(B, \Omega_i)\, k_{ij}(B). \tag{21}$$

Here, the modulation frequency Ω as well as a function $f_{ij}(B, \Omega)$ depend not only on the EPR transition branch but also on the location of the nucleus which is given by the dipolar frequency and the unit vector $\mathbf{r}$. At a fixed magnetic field, the field-selected ESEEM response may therefore contain contributions from more than one transition branch and from a range of molecular orientations when the corresponding resonance regions overlap. This should be taken into account when assigning spectral features to individual turning points.

Obviously, integrating the function $f_{ij}(B, \Omega)$ over the nuclear frequencies gives the function $f_{ij}(B)$, which is proportional to the intensity of the corresponding EPR line (8). Thus, the Fourier analysis of the experimental data provides valuable information about the HFI and the nucleus's relative position with respect to the paramagnetic particle. In the case of a spin-polarized triplet state, ESEEM spectra can also provide additional information about the signs of the ZFS and the electron spin polarization which is not available from the TREPR method.

3. Results and Discussion

3.1. Turning Points

Within the high-field approximation $\omega_{\text{T}} \gg |D|, |E|$, the energy gaps between the triplet sublevels equal (see Appendices B and C):

$$\Delta E_{\pm} = \omega_{\text{T}} \pm d = \omega_{\text{T}} \mp (D/2)\left(1 - 3\cos^2\theta\right) \pm (3E/2)\sin^2\theta\cos 2\varphi. \tag{22}$$

Here θ and φ are the polar and azimuthal angles defining the direction of the external magnetic field in the ZFS tensor frame (49).

The spin polarization has a similar form:

$$\begin{gathered} \Delta p_{\pm} = \pm p_{\parallel}\left(1 - 3\cos^2\theta\right)/2 \mp (3p_{\perp}/2)\sin^2\theta\cos 2\varphi, \\ p_{\parallel} = p_Z - (p_X + p_Y)/2, \\ p_{\perp} = (p_X - p_Y)/2. \end{gathered} \tag{23}$$

Due to the angular dependence of the electron spin wave function and the direction of the unit vector $\mathbf{r} \equiv (r_x, r_y, r_z)$, the expressions for the effective field and, consequently, the modulation frequency and modulation depths, are difficult to analyze analytically. However, the situation changes substantially when the external field is along one of the ZFS principal axes. We now consider these cases explicitly. There are two EPR transitions $\psi_{+1} \leftrightarrow \psi_0$ and $\psi_{-1} \leftrightarrow \psi_0$ corresponding to each of these orientations. The resonance fields of these transitions are symmetric relative to the central point B_0 (10):

$$B_{\pm(\xi=X,Y,Z)} = B_0 \pm \Delta B_{\xi}. \tag{24}$$

We denote these resonance fields as turning points. Equation (24), as well as the definition of the central field B_0 in eq. (10), is written within the isotropic g-factor approximation. In the general case, the Zeeman term contains an anisotropic g-tensor, and the effective Zeeman splitting is determined by the orientation-dependent value g_{eff}. Accordingly, the central field also becomes orientation dependent. At the turning points, this corresponds to $B_{0,\xi} = \hbar\omega_{\text{MW}}/(\beta_{\text{e}} g_{\text{eff},\xi})$, where $g_{\text{eff},\xi}$ is the effective g-value for the molecular orientation with the magnetic field along the ξ axis. In the analytical treatment below, we retain the scalar g-factor approximation in order to keep the expressions compact and to examine the ZFS contribution to the resonance-field offsets. The formalism can be extended to the anisotropic case by replacing g and B_0 with the corresponding orientation-dependent quantities. For a given orientation, the shift ΔB_ξ can be found by solving the eqs. (5) for the spin Hamiltonian (1):

$$\begin{aligned} \Delta B_X = \Delta B(\theta = \pi/2, \varphi = 0) = (\hbar/g\beta_{\text{e}})(D - 3E)/2, \\ \Delta B_Y = \Delta B(\theta = \pi/2, \varphi = \pi/2) = (\hbar/g\beta_{\text{e}})(D + 3E)/2, \\ \Delta B_Z = \Delta B(\theta = 0) = -(\hbar/g\beta_{\text{e}})D. \end{aligned} \tag{25}$$

The splitting of the nuclear spin sublevels at $m = 0$ corresponds to the nuclear Zeeman frequency. Therefore, at the turning points, it can be reformulated using the central frequency and the difference between two frequencies corresponding to the two EPR transitions:

$$\Omega_{\pm 0,(\xi=X,Y,Z)} = |\omega_{\pm 0,\xi}| \tag{26}$$

with

$$\omega_{\pm 0,\xi} = \omega_0 \pm \Delta\omega_\xi = \gamma_{\text{n}}(B_0 \pm \Delta B_\xi). \tag{27}$$

The mixing of the laboratory frame wave functions is minimal when the external magnetic field is aligned with the ZFS's principal axes. Expressions (54) and (55) (Appendix C) show that within the linear approximation used to derive the expectation values, $\langle S_{x,y} \rangle = 0$. Indeed, when the direction of external field is along the principal axes the angles θ, φ have values of 0 or $\pi/2$. Therefore, $\sin 2\theta = \sin 2\varphi = 0$ and $\langle S_{x,y} \rangle = 0$. This property simplifies the description of ESEEM properties. Another simplification at turning points is due to the fact that the direction cosines of the laboratory and molecular frames have a very simple relationship. As a result, the ESEEM frequencies formed by the nuclear spin coherences for $m = \pm 1$ are given by

$$\Omega_{\pm 1,(\xi=X,Y,Z)} = \left[\left(\omega_{\text{dd}}(3r_\xi^2 - 1) + \omega_{\text{iso}} \mp \omega_{\pm 0,\xi} \right)^2 + 9\omega_{\text{dd}}^2 r_\xi^2 (1 - r_\xi^2) \right]^{1/2}. \tag{28}$$

Here, r_ξ is the component of the radius vector $\mathbf{r}$ determined in the molecular frame. The modulation depths for the ESEEM signal in branches $\psi_{+1} \leftrightarrow \psi_0$ and $\psi_{-1} \leftrightarrow \psi_0$ are equal to

$$k_{\pm(\xi=X,Y,Z)} = 1 - \frac{\left(\omega_{\text{dd}}(3r_\xi^2 - 1) + \omega_{\text{iso}} \mp \omega_{\pm 0,\xi} \right)^2}{\Omega_{\pm 1,\xi}^2}. \tag{29}$$

Note that the direction cosines in expressions (28)-(29) are determined in the molecular frame. Thus, they provide direct information about the location of the nucleus with respect to the molecular frame.

These expressions demonstrate that both the frequency and the modulation depth depend on the EPR transition branch. As discussed above, the transition probabilities and resonance conditions at the two branches are nearly the same. Thus, comparison of the two branches

provides constraints on the strengths of the electron-nuclear interactions and on the orientation of the dipolar coupling.

In particular, the difference in the squares of the Ω-values

$$\Delta\Omega_{\xi}^{(2)} = \Omega_{+\xi}^2 - \Omega_{-\xi}^2 = -4\omega_0 \left(\omega_{\mathrm{dd}}(3r_{\xi}^2 - 1) + \omega_{\mathrm{iso}} - \Delta\omega_{\xi}\right) \tag{30}$$

shows how the frequency shift depends on the orientation of the vector connecting unpaired electrons and nucleus. When the value of $\Delta\omega_{\xi}$ (26) is small, the frequency shift along the selected axis correlates with the direction cosine in that direction.

The difference in the k-values

$$\Delta k_{\xi} = k_{+\xi} - k_{-\xi} \tag{31}$$

is more complicated. At turning points, the expression (31) is zero when the dipolar axis is collinear with one of the ZFS principal axes: $\Delta k_{\xi=X,Y,Z}(r_{\xi} = 0) = \Delta k_{\xi}(r_{\xi} = 1) = 0$. Thus, the difference in modulation depths does not provide an unambiguous result. However, examining the parameter Δk allows one to estimate the approximate direction of the dipolar coupling.

When the variation of the nuclear Zeeman frequencies across the spectrum is negligible ($\omega_{\mathrm{n}} \gg \Delta\omega$), the difference in the k-values depends only on the ratios $\omega_{\mathrm{dd}}/\omega_{\mathrm{n}}$ and $\omega_{\mathrm{iso}}/\omega_{\mathrm{n}}$. Figure 2 illustrates the behavior of the normalized function $\Delta k_{\xi}\,(\omega_{\mathrm{n}}/\omega_{\mathrm{dd}})^2$ at fixed values of the HFI contributions, for the typical case in which the Zeeman interaction dominates, $|\omega_{\mathrm{n}}| > |\omega_{\mathrm{dd}}|, |\omega_{\mathrm{iso}}|$. Under these conditions, $\Delta k_{\xi} < 0$ when the external magnetic field is nearly parallel to the dipolar coupling axis ($r_{\xi} \to 1$), whereas $\Delta k_{\xi} > 0$ when the two are more orthogonal ($r_{\xi} \to 0$).

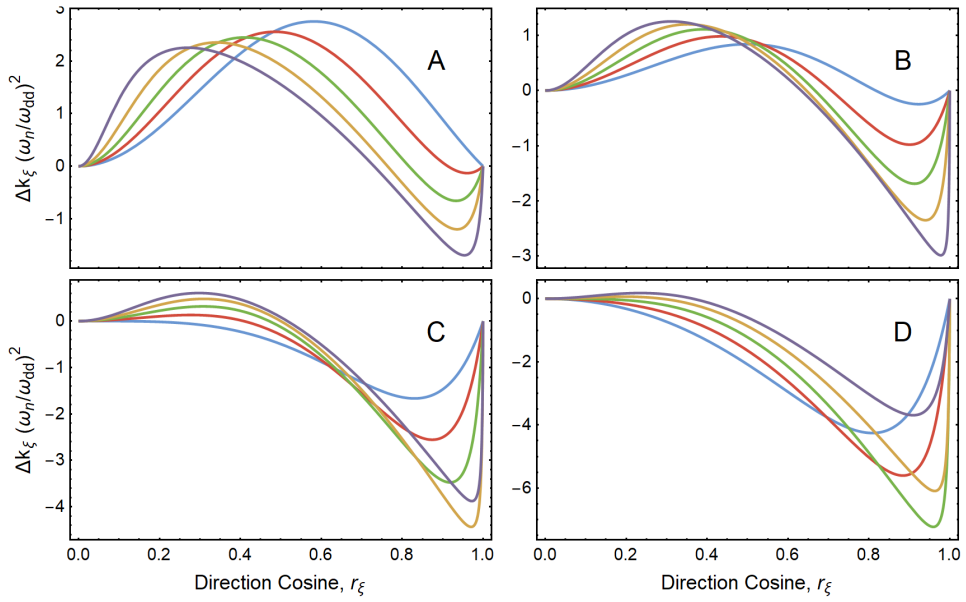

Figure 2. Ratio $\Delta k_{\xi}\,(\omega_{\mathrm{n}}/\omega_{\mathrm{dd}})^2$ as a function of the nuclear spin interaction parameters. This function is independent of the value ω_{n} (see text). The HFI parameters are: $\omega_{\mathrm{iso}}/\omega = -0.3$ (panel A), -0.1 (panel B), 0.1 (panel C), 0.3 (panel D); $\omega_{\mathrm{dd}}/\omega = 0.1$ (blue), 0.2 (red), 0.3 (green), 0.4 (sand), 0.5 (purple).

3.2. Modulation Depth Analysis

The asymmetry in the modulation frequencies $\Delta\Omega_{\xi}^{(2)}$ is directly related to the nuclear spin sublevels. It has a very simple form (30). Thus, studying the nuclear spin frequencies at specific

points using hyperfine spectroscopy, especially ENDOR spectroscopy, can provide valuable information about HFI parameters, including the HFI tensor orientation. Compared to ENDOR, the spectral resolution of ESEEM experiments is generally less accurate. However, unlike ENDOR, ESEEM provides additional insight by examining the differences in modulation depths. In particular, eq. (31) enables the classification of HFI properties based on the intensity asymmetries observed in 2D field-swept ESEEM spectra. This expression allows one to estimate nuclear magnetic parameters from the ESEEM signal intensity at special magnetic-field positions, accounting for population differences in transitions at $B_{\rm res} = B_0 \pm \Delta B_\xi$.

3.2.1. Limiting case $\omega_{\rm dd} \ll \omega_{\rm n}$

In the limiting case of $\omega_{\rm dd} \ll \omega_{\rm n}$, we have:

$$\Delta k_\xi \approx \frac{36\omega_{\rm dd}^2(\Delta\omega_\xi - \omega_{\rm iso})\omega_0\, r_\xi^2(1-r_\xi^2)}{\left(\omega_0^2 - (\Delta\omega_\xi - \omega_{\rm iso})^2\right)^2}, \tag{32}$$

and therefore:

$$\operatorname{sign}(\Delta k_\xi) = \operatorname{sign}\big[\omega_0(\Delta\omega_\xi - \omega_{\rm iso})\big]. \tag{33}$$

The signs of the frequencies ω_0, $\Delta\omega_\xi$ and $\omega_{\rm dd}$ are determined by the sign of the nuclear gyromagnetic ratio $\gamma_{\rm n}$, whereas the sign of $\omega_{\rm iso}$ also depends on the electron spin density at the nucleus.

When $|\omega_0| > |\omega_{\rm iso}| > |\Delta\omega_\xi|$ the expression (33) reduces to $\operatorname{sign}(\Delta k) = -\operatorname{sign}(\omega_0 \cdot \omega_{\rm iso})$, implying that the modulation depth asymmetry directly reflects the sign of the isotropic hyperfine contribution $\omega_{\rm iso}$. The comparison of the blue curves in Fig. 2 ($\omega_{\rm dd}/\omega_{\rm n} = 0.1$) illustrates this behavior.

The rest of this section describes the situation when the isotropic HFI contribution is negligible ($\omega_{\rm iso} = 0$). Additional examples illustrating the influence of the isotropic interaction are presented in the following section.

For $\omega_{\rm iso} = 0$, eq. (26) gives

$$\operatorname{sign}(\Delta k_\xi) = \operatorname{sign}(\Delta B_\xi). \tag{34}$$

In this case, the sign of the ZFS parameter D is directly related to the difference in modulation depths observed at turning points.

Assuming $D > 0$ (a change in the sign of D reverses the intensity ordering), eq. (25) yields $\Delta B_X > 0$. Consequently, $k_{+X} = k(B_0 + \Delta B_X) > k_{-X} = k(B_0 - \Delta B_X)$, and the modulation depth of the high-field branch exceeds that of the low-field branch:

$$k_X(B_{\rm res} < B_0) < k_X(B_{\rm res} > B_0). \tag{35}$$

Analogously,

$$k_Y(B_{\rm res} < B_0) < k_Y(B_{\rm res} > B_0), \tag{36}$$

whereas

$$k_Z(B_{\rm res} < B_0) > k_Z(B_{\rm res} > B_0). \tag{37}$$

Caution is required when applying eqs. (35)–(37), because as discussed above, maximal intensities do not always appear at turning points. Additionally, the signal intensity at $B_{\rm res} = B_{\pm Z}$ is often weaker than at other turning points. Therefore, a more accurate comparison between different orientations may require correction for population differences. As illustrated in Fig. 3, the orientation of the dipolar axis significantly influences the 2D ESEEM spectrum. Figure 4

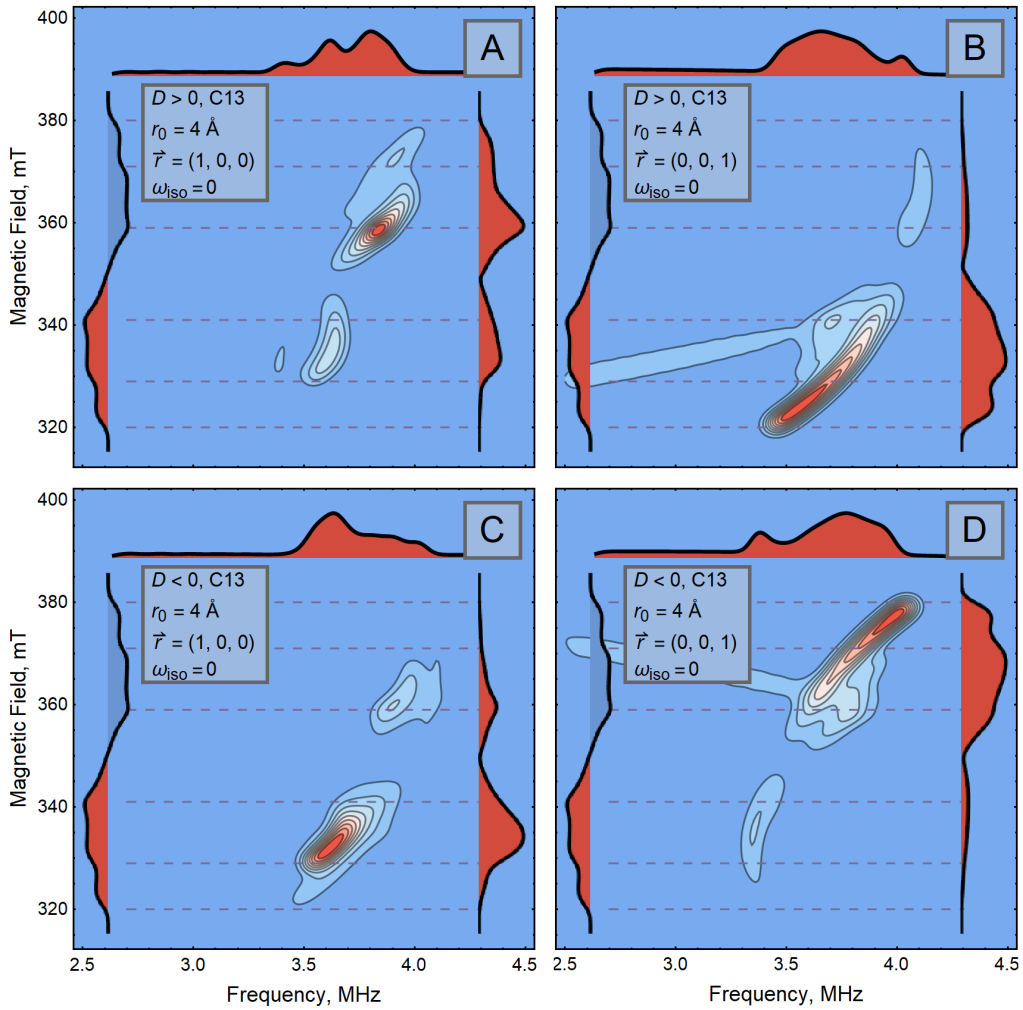

Figure 3. The calculated 2D ESEEM spectra of the triplet state, along with additional spectra shown in red. The TREPR spectrum is on the left, the 2D ESEEM spectra integrated over the magnetic field are on the top, and the 2D ESEEM spectra integrated over the modulation frequencies are on the right. The color scale ranges from blue to red, indicating the intensity from minimum to maximum. Simulation parameters: $p_Z > 0$, $D = +30\,\text{mT}$ (841 MHz), $\mathbf{r} = (1,0,0)$ (panel A), $p_Z > 0$, $D = +30\,\text{mT}$ (841 MHz), $\mathbf{r} = (0,0,1)$ (panel B), $p_Z < 0$, $D = -30\,\text{mT}$ (-841 MHz), $\mathbf{r} = (1,0,0)$ (panel C), $p_Z < 0$, $D = -30\,\text{mT}$ (-841 MHz), $\mathbf{r} = (0,0,1)$ (panel D). The other parameters are the same for all panels: $p_{X,Y} = 0$, $E = 4\,\text{mT}$ (112 MHz), $r_0 = 4\,\text{Å}$, $\omega_{\text{iso}} = 0$.

further examines the dependence of spectral patterns on the dipolar axis. Note that the calculations use the unit vector $\mathbf{r}$, whereas subsequent figures, including Fig. 4, present these vectors in a shorter, non-normalized form. For example, $\mathbf{r} = (1,1,0)$ should be read as $\mathbf{r} = (1,1,0)/\sqrt{2}$.

The simulations confirm the relationships predicted by the analytical expressions. The asymmetry of the peak intensities is inverted when the sign of D is changed, as shown in eqs. (25) and (34). This situation is illustrated in Fig. 3. The figure shows several model 2D ESEEM spectra corresponding to the Fourier-domain representation of three-pulse ESEEM. The spectra were calculated for a ^{13}C nucleus located 4 Å away from the triplet electron spin. The intensity of the peaks is scaled from blue (minimum) to red (maximum). For comparison, the TREPR spectrum of the triplet is shown on the left side of each 2D ESEEM spectrum, and the field positions corresponding to the turning points are indicated by dashed lines. In addition, 1D projections obtained by integrating over the magnetic field and the modulation frequencies intervals,

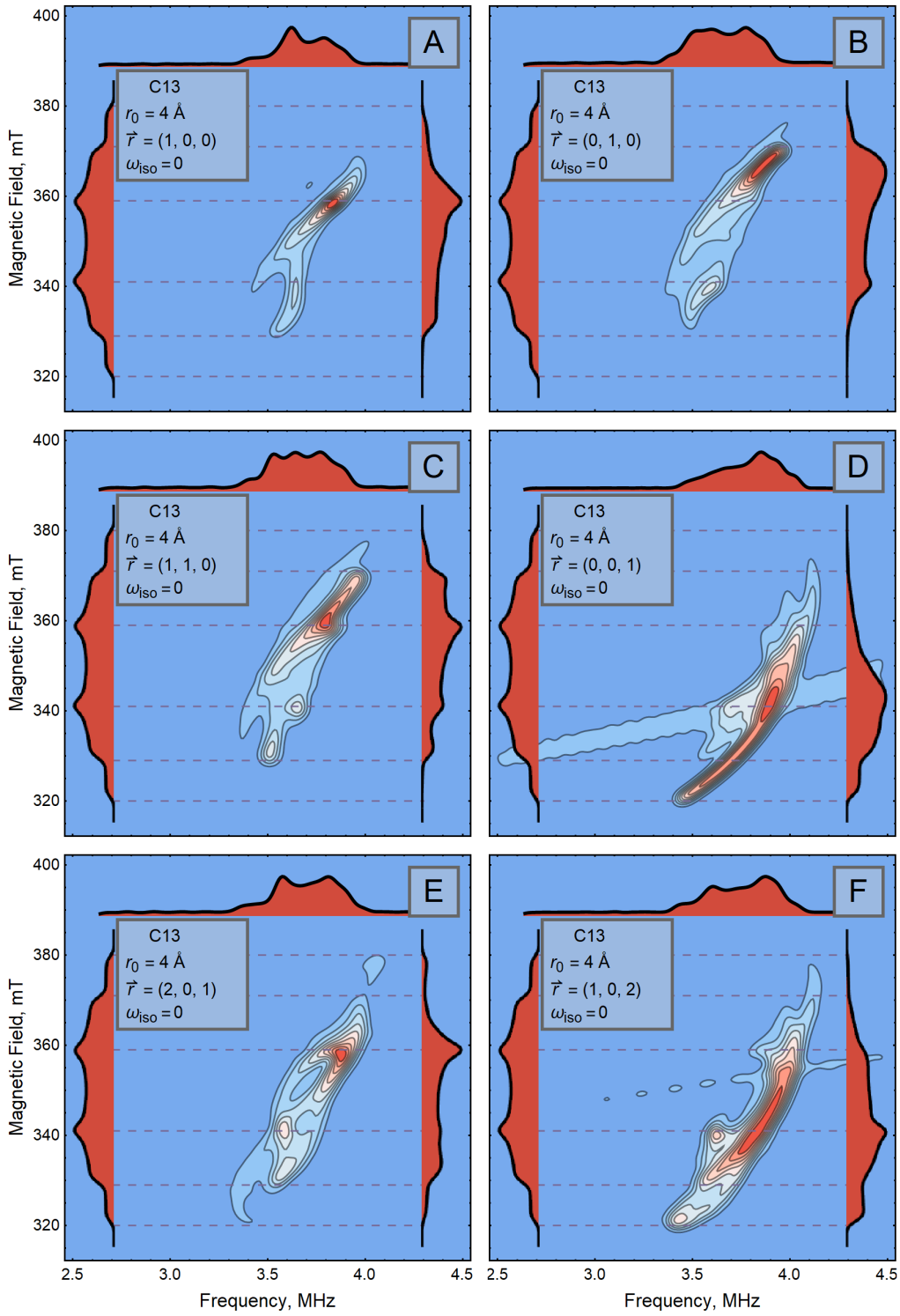

Figure 4. The calculated 2D ESEEM spectra of the triplet state, along with additional spectra shown in red. The TREPR spectrum is on the left, the 2D ESEEM spectra integrated over the magnetic field are on the top, and the 2D ESEEM spectra integrated over the modulation frequencies are on the right. The color scale ranges from blue to red, indicating the intensity from minimum to maximum. Simulation parameters equal: $p_Z > 0$, $D = +30\,\mathrm{mT}$ (841 MHz), $E = 4\,\mathrm{mT}$ (112 MHz), $r_0 = 4\,\text{Å}$, $\omega_{\mathrm{iso}} = 0$. The relative orientation of the dipolar axis: $\mathbf{r} = (0,0,1)$ (panel A), $\mathbf{r} = (0,1,0)$ (panel B), $\mathbf{r} = (1,1,0)/\sqrt{2}$ (panel C), $\mathbf{r} = (0,0,1)$ (panel D), $\mathbf{r} = (2,0,1)/\sqrt{5}$ (panel E), $\mathbf{r} = (1,0,2)/\sqrt{5}$ (panel F).

respectively, are presented on the top and right sides of the ESEEM spectrum.

Two types of triplet states are analyzed: 1) $D > 0$, $p_Z > 0$, and $p_{X,Y} = 0$ (panels A and B), and 2) $D < 0$, $p_Z < 0$, and $p_{X,Y} = 0$ (panels C and D). Due to $\mathrm{sign}(D\,p_Z) > 0$ for both sets, they have the same TREPR pattern. However, the ESEEM has spectra with different structures because the modulation depth is sensitive to the sign of ZFS parameter D, but not to the sign of the spin polarization p_Z. The dependence on the orientation of the HFI tensor is also evident. Panels A and C show the spectra for a dipole axis oriented along the X-axis of the molecular frame ($\mathbf{r} = (1, 0, 0)$), and panels B and D show the spectra for a dipole axis oriented along the Z-axis of the molecular frame ($\mathbf{r} = (0, 0, 1)$). A change in the sign of D leads to a reversal of the spectral properties. Note that the spectra at $D > 0$ and $D < 0$ have almost inverse symmetry but not complete one. These differences arise from the nonlinear dependence of the modulation frequency and modulation depth on the magnetic field offset, ΔB.

For simplicity, hereafter the HFI parameters are given in MHz rather than angular-frequency units. The zero-field splitting parameters D and E are provided both in frequency (MHz) and in magnetic-field (mT).

Two main conclusions can be drawn from the results presented in Fig. 4.

First, model calculations show that the signal intensity near $B_{\mathrm{res}} \approx B_Y$ correlates less strongly with the direction cosine r_Y than at other turning points. The spectra calculated for $r_Y \approx 1$ closely resemble those obtained for $r_X \approx 1$. For comparison, Fig. 4B was calculated using the same parameters as Fig. 4A, except r_Y was set to 1 instead of r_X. This behavior occurs because molecules that resonate near $B_{\mathrm{res}} \approx B_{X,Z}$ correspond to the extrema of the principal values and are localized within narrow angular ranges. This leads to constructive interference of their oscillations. In contrast, molecules contributing near $B_{\mathrm{res}} \approx B_Y$ are distributed over a broader angular range. This results in partial destructive interference and reduced contributions from these transitions. This limited orientation selectivity is especially relevant when the B_X and B_Y turning points are close in field, because the contributions associated with the $B \parallel X$ and $B \parallel Y$ orientations may then significantly overlap. Second, a relatively large value $r_\xi^2(1 - r_\xi^2)$ is required to produce a detectable signal near $B_{\mathrm{res}} \approx B_Z$. Unlike at other points, the ESEEM signal at this position is very weak when r_Z is small.

The spectra shown in Figs. 3 and 4 were calculated for $\omega_{\mathrm{iso}} = 0$. The model calculations show that, when the isotropic interaction becomes comparable to the dipolar coupling, the relationship between the direction cosines and the modulation depth becomes more complex. Notably, the sign of Δk obtained for $\omega_{\mathrm{iso}} = 0$ may change if ω_{iso} and ω_{dd} have opposite signs.

3.2.2. Limiting case $\omega_{\mathrm{n}} \ll \omega_{\mathrm{dd}}$

When $\omega_{\mathrm{n}} \ll \omega_{\mathrm{dd}}$, the modulation depths behave more complexly and exhibit a more explicit dependence on the dipolar coupling orientation:

$$\Delta k_\xi \approx -\frac{36\omega_{\mathrm{dd}}^2 r_\xi^2(1 - r_\xi^2)\left(\omega_{\mathrm{dd}}(3r_\xi^2 - 1) + \omega_{\mathrm{iso}}\right)\omega_0}{\left(\left(\omega_{\mathrm{dd}}(3r_\xi^2 - 1) + \omega_{\mathrm{iso}}\right)^2 + 9\omega_{\mathrm{dd}}^2 r_\xi^2(1 - r_\xi^2)\right)^2}. \tag{38}$$

For $\omega_{\mathrm{iso}} = 0$, one finds

$$\mathrm{sign}(\Delta k_\xi) = -\,\mathrm{sign}(3r_\xi^2 - 1). \tag{39}$$

For $D > 0$ we have $\Delta B_X > 0$ (see Fig. 1), and the modulation depth satisfies

$$k_X(B_{\mathrm{res}} < B_0) > k_X(B_{\mathrm{res}} > B_0) \quad \text{for} \quad 3r_X^2 > 1 \tag{40}$$

and

$$k_X(B_{\rm res} < B_0) < k_X(B_{\rm res} > B_0) \quad \text{for} \quad 3r_X^2 < 1. \tag{41}$$

Similar relations can be derived for the other turning points.

In general, the distribution of ESEEM frequencies is wider in the case of $\omega_{\rm n} < \omega_{\rm dd}$ than in the case of $\omega_{\rm n} > \omega_{\rm dd}$, a property that might help differentiate these two cases in the analysis of experimental data.

3.3. Application to $Y_3N@C_{80}$

3.3.1. Experimental methods

The $Y_3N@C_{80}$ endofullerenes were provided by Dr. A. Popov (IFW Dresden, Germany). For the EPR experiments, the endofullerene was dissolved in decalin (a mixture of *cis*- and *trans*-isomers).

The EPR measurements were performed using a Bruker Elexsys E580 spectrometer equipped with a commercially available ER4118MD5-W1 resonator. Temperature control was achieved using an ITC503 temperature controller (Oxford Instruments). All measurements were carried out at 50 K. A continuous-wave laser (532 nm, 200 mW) was used as the light source.

Echo-detected EPR spectra were recorded using a standard two-pulse sequence with a fixed delay time τ between the two microwave pulses. The $\pi/2$ pulse length was 10 ns, and the interpulse delay was 130 ns.

2D ESEEM measurements were performed using a stimulated echo pulse sequence ($\pi/2 - \tau - \pi/2 - T - \pi/2 - \tau -$ echo) with the echo amplitude recorded as a function of the delay time T. The $\pi/2$ pulse length was 16 ns, and the delay time T was varied from 340 ns to 8 μs. The interpulse delay time τ was set to 1370 ns to maximize the modulation depths for both ^{89}Y and naturally abundant ^{13}C nuclei.

3.3.2. Results

The endofullerene $Y_3N@C_{80}$ contains three magnetically equivalent yttrium nuclei ($I = 1/2$) and one ^{14}N ($I = 1$). Upon light excitation, the fullerene forms a metastable triplet state whose properties are well established [32]. The zero-field splitting (ZFS) tensor is essentially axial, with $D \approx +128$ MHz (4.6 mT), $E \approx 0$, and the principal Z-axis is oriented normal to the fullerene cage surface. The principal values of the g-tensor of the triplet state equal $g_x = 2.0004$, $g_y = 2.0008$, $g_z = 2.0030$ [32].

The echo-detected EPR spectrum of $Y_3N@C_{80}$ under continuous light excitation is shown in the inset of Fig. 5. It should be noted that under continuous optical excitation, the populations of the spin sublevels remain close to thermal equilibrium. Consequently, the density matrix of the triplet state is approximated in the high-temperature regime as $\rho \sim S_{{\rm T},z}$.

The vertical lines correspond to the resonance fields near the turning points $B_{\pm X} \approx B_{\pm Y}$ and $B_{\pm Z}$. The main panel shows the time dependence of the ESEEM signal at these positions. The data clearly demonstrate oscillations with two distinct frequencies. These frequencies are separated well in the Fourier transform spectrum of the 2D ESEEM data shown in Fig. 6. The frequencies are close to the nuclear Zeeman frequencies of the yttrium ^{89}Y and ^{13}C nuclei. No signal associated with the ^{14}N nucleus is detected in the present ESEEM experiment.

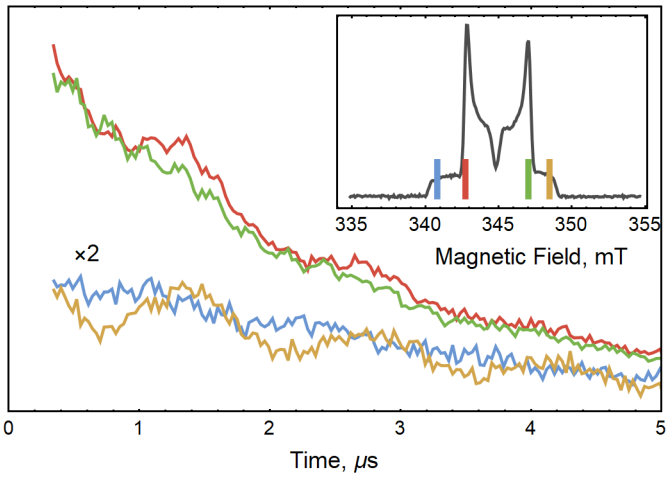

Figure 5. ESEEM traces of photoexcited $Y_3N@C_{80}$ at selected magnetic field values. The echo-detected EPR spectrum of $Y_3N@C_{80}$ under continuous light excitation is displayed in the inset. Vertical lines mark the magnetic field positions at which the ESEEM signals were acquired. These positions are close to the turning points $B_{\pm Z}$ (blue and sand) and $B_{\pm X} = B_{\pm Y}$ (green and red). For clarity, the blue and sand traces are enlarged by a factor of two.

3.3.3. Simulations

The low-frequency part of the spectrum is induced by the coherences of the nuclear spin of ^{89}Y ($\nu \approx 0.7$ MHz). To model the experimental data, the HFI was approximated by point dipole interaction with the distance $r_0 = 3.5$ Å($\omega_{dd}/2\pi = -0.56$ MHz). We emphasize that the point-

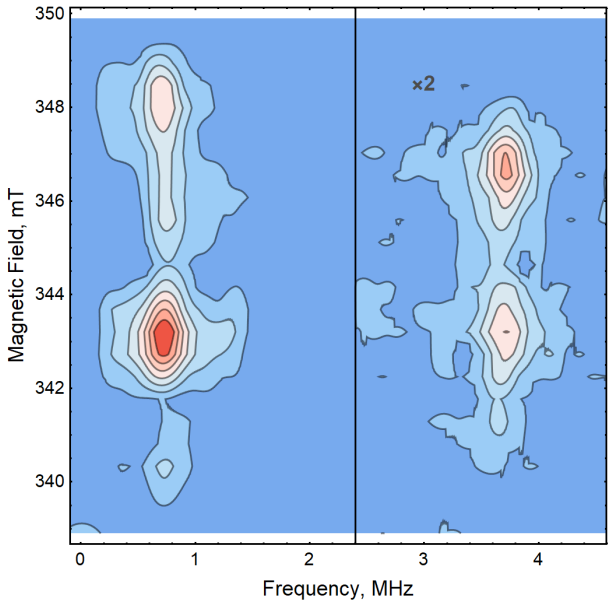

Figure 6. Two-dimensional ESEEM spectrum of $Y_3N@C_{80}$. The left part of the spectrum ($\nu \approx 0.7$ MHz) corresponds to the ^{89}Y signal, while the right part ($\nu \approx 3.7$ MHz) corresponds to the ^{13}C signal. Spectral intensity is scaled from minimum (0) to maximum using a blue-to-red color scale. The intensity on the right side of the panel, starting at 2.4 MHz, is magnified by a factor of two.

dipole approximation used here provides only effective HFI parameters. A detailed spin-density distribution for the triplet state of $Y_3N@C_{80}$ was calculated in [32] and shown in Fig. 2b of that work. However, delocalization of the electron spin density over the fullerene cage and the

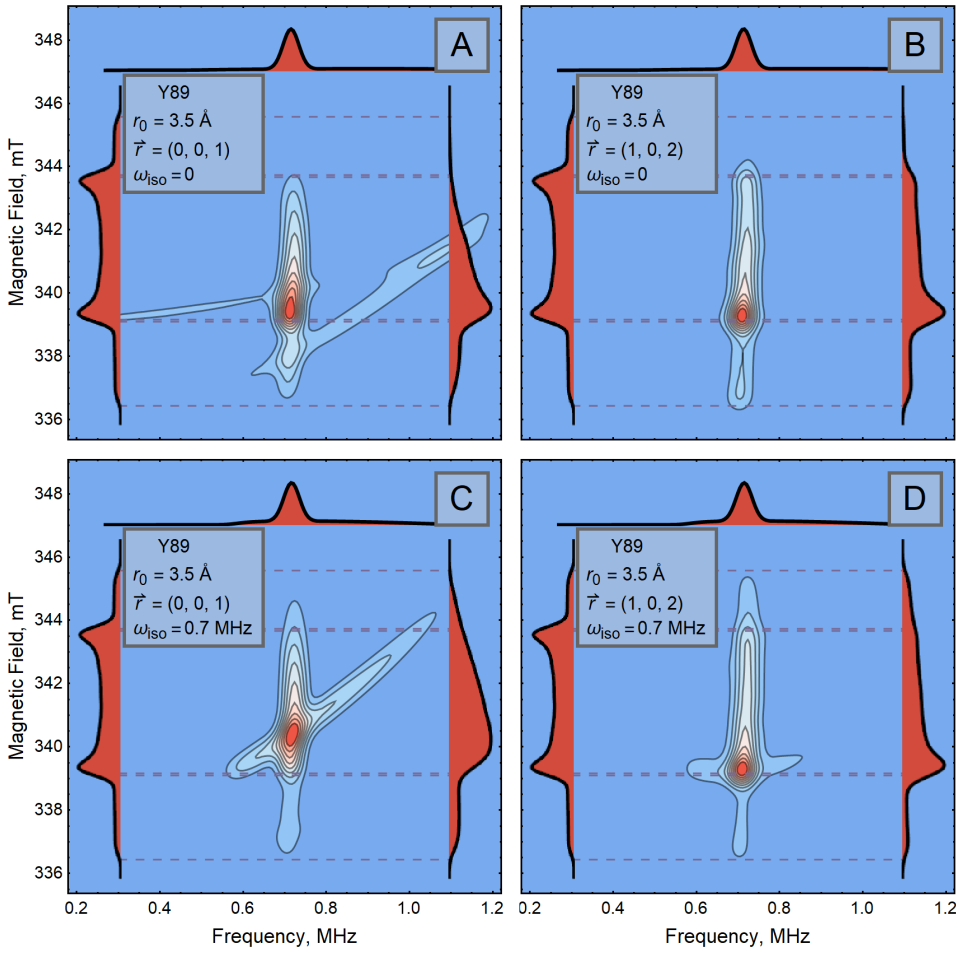

Figure 7. The calculated 2D ESEEM spectra formed by the ^{89}Y nucleus, along with additional spectra shown in red. The TREPR spectrum is on the left, the 2D ESEEM spectra integrated over the magnetic field are on the top, and the 2D ESEEM spectra integrated over the modulation frequencies are on the right. The color scale ranges from blue to red, indicating the intensity from minimum to maximum. Simulation parameters: $\omega_{\rm iso} = 0$, $\mathbf{r} = (0, 0, 1)$ (panel A), $\omega_{\rm iso} = 0$, $\mathbf{r} = (1, 0, 2)/\sqrt{5}$ (panel B), $\omega_{\rm iso}/2\pi = 0.7\,$MHz, $\mathbf{r} = (0, 0, 1)$ (panel C), $\omega_{\rm iso}/2\pi = 0.7\,$MHz, $\mathbf{r} = (1, 0, 2)/\sqrt{5}$ (panel D). The other parameters: $g_x = 2.0004$, $g_y = 2.0008$, $g_z = 2.0030$, $D = 128\,$MHz (4.6 mT), $E = 0$, $r = 3.5\,$Å.

random distribution of naturally abundant magnetic ^{13}C nuclei preclude extracting accurate HFI tensors from the present ESEEM data. This value was estimated based on the mean radius of the C_{80} fullerene cage (4 Å). Simulations with $\omega_{\rm iso} = 0$ cannot reproduce the modulation depth relationship (Δk-values). This is not surprising, considering the results presented in Figs. 4 and 6. Several simulations of ^{89}Y with different HFIs are provided in Fig. 7.

A comparison of Figs. 6 and 7 shows that the ESEEM data can be reasonably explained by a non-radial dipolar coupling axis ($r_{X,Y} \neq 0$) and $\omega_{\rm iso}/2\pi = 0.7\,$MHz. This value is comparable with the value +1.02 MHz found in combined EPR/ENDOR/DFT studies [32].

The high-frequency portion of the 2D spectrum (Fig. 6) is induced by coherences of nuclear spins of ^{13}C ($\nu \approx 3.7\,$MHz). The properties of the HFI of the triplet state with the in-surface ^{13}C nuclei are unknown. To model ESEEM data, point dipole interaction with the distance $r_0 = 3.5\,$Å($\omega_{\rm dd}/2\pi = 2.88\,$MHz) is used. Several data sets computed with different HFI values are presented in Fig. 8.

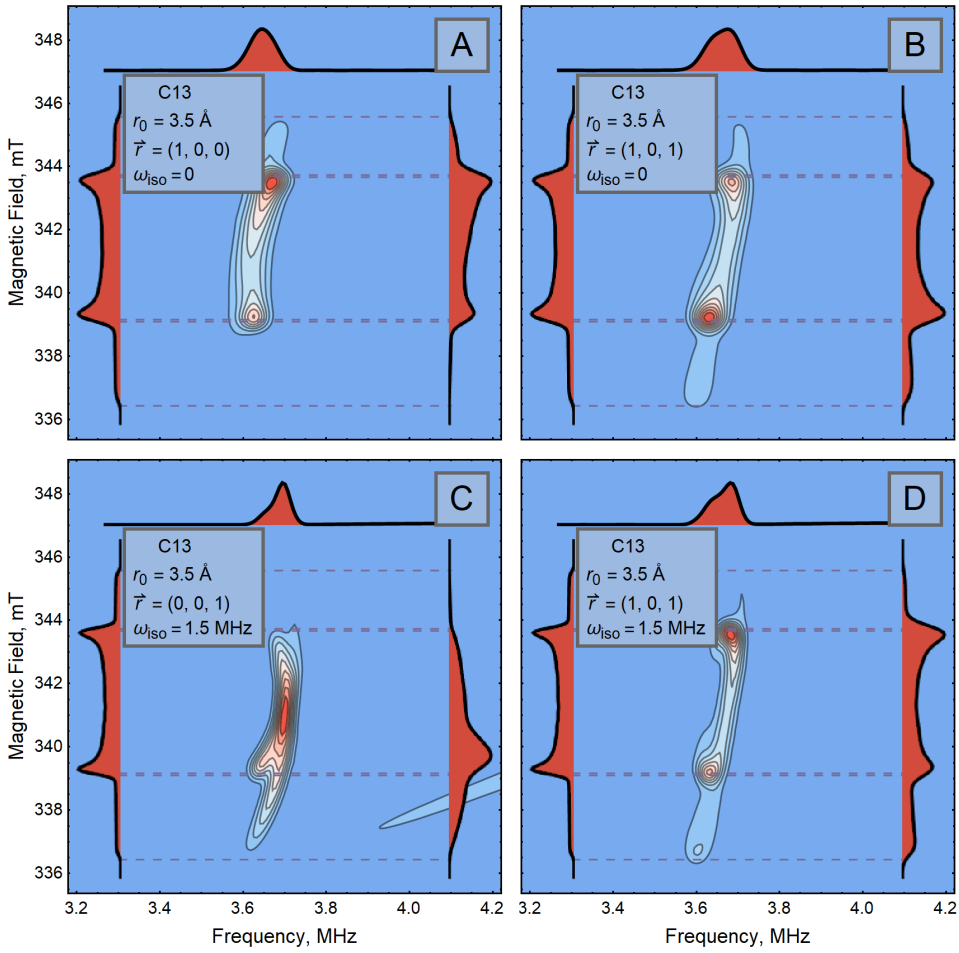

Figure 8. The calculated 2D ESEEM spectra formed by the ^{13}C nucleus, along with additional spectra shown in red. The TREPR spectrum is on the left, the 2D ESEEM spectra integrated over the magnetic field are on the top, and the 2D ESEEM spectra integrated over the modulation frequencies are on the right. The color scale ranges from blue to red, indicating the intensity from minimum to maximum. Simulation parameters: $\omega_{\text{iso}} = 0$, $\mathbf{r} = (1, 0, 0)$ (panel A), $\omega_{\text{iso}} = 0$, $\mathbf{r} = (1, 0, 1)/\sqrt{2}$ (panel B), $\omega_{\text{iso}}/2\pi = 1.5\,\text{MHz}$, $\mathbf{r} = (0, 0, 1)$ (panel C), $\omega_{\text{iso}}/2\pi = 1.5\,\text{MHz}$, $\mathbf{r} = (1, 0, 1)/\sqrt{2}$ (panel D). The other parameters: $g_x = 2.0004$, $g_y = 2.0008$, $g_z = 2.0030$, $D = 128\,\text{MHz}$ (4.6 mT), $E = 0$, $r = 3.5$ Å.

A comparison of Figs. 6 and 8 shows that the ESEEM data can be modeled with $\omega_{\text{iso}}/2\pi = 1.5\,\text{MHz}$ and a significant in-plane contribution of dipole coupling. The observation of the ESEEM signal at $B_{\text{res}} \sim B_{\pm Z}$ indicates the presence of an out-of-surface contribution, too. Simulations show that a reasonable spectral pattern is obtained with an average direction of $\mathbf{r} = (1, 0, 1)$ (Fig. 8D). However, the experimental data can also be interpreted differently by assuming that the ESEEM signals are formed by ^{13}C nuclei with different locations in the fullerene cage, which have different dipolar coupling axes. In particular, combining the spectra shown in Figs. 4A and 4D can produce an ESEEM pattern similar to that observed in the experiment (right part of Fig. 6).

In total, the differences in the resonance frequencies $\Delta\Omega$ and the modulation depths Δk derived at turning points for the two branches $\psi_{+1} \leftrightarrow \psi_0$ and $\psi_{-1} \leftrightarrow \psi_0$ provide useful information about the relationship between dipole-dipole and Fermi contact interaction parameters. The comparison of the experimental ESEEM data with the simulations allows one to estimate

the mean direction of the dipole axis. The 2D ESEEM data recorded for $Y_3N@C_{80}$ are in reasonable agreement with the results obtained earlier by different methods.

4. Conclusions

An analytical framework for describing ESEEM in spin-polarized triplet states has been developed and applied to two-dimensional ESEEM experiments on powder samples. The analysis shows that, at resonance positions associated with the principal axes of the ZFS tensor, the two allowed EPR transitions exhibit distinct nuclear modulation frequencies and modulation depths. These differences provide access to the sign of the ZFS parameter D and to the relative contributions of isotropic and dipolar HFIs.

Numerical simulations confirm the analytical predictions and illustrate how the interplay between ZFS anisotropy, non-equilibrium spin polarization, and anisotropic HFI determines the structure of the 2D ESEEM spectra. Application of the developed approach to the photoexcited triplet state of $Y_3N@C_{80}$ demonstrates that the experimental data can be consistently reproduced with $D > 0$ by including both isotropic and dipolar hyperfine couplings and by allowing for non-collinear orientations of the dipolar interaction relative to the ZFS axes.

Overall, the present results show that 2D ESEEM can serve as a useful complement to TREPR in the characterization of photoexcited triplet states. Within the present framework, the method provides access to the sign of the ZFS interaction and to selected spatial characteristics of hyperfine couplings.

Acknowledgments

The authors are grateful to Dr. A. Popov (IFW Dresden, Germany) for providing the $Y_3N@C_{80}$ endofullerene. The work of Y.E.K. was carried out at the expense of a grant provided by the Academy of Sciences of the Republic of Tatarstan to higher education institutions, scientific and other organizations, to support human resources development plans in the part concerning the stimulation of their scientific and scientific-pedagogical staff to defend Doctor of Science dissertations and to carry out research work. R.B.Z. acknowledges the financial support from the government assignment for FRC Kazan Scientific Center of RAS and thanks the Center for Collective Use for Studying the Structure, Composition, and Properties of Substances and Materials of FRC of Kazan Scientific Center of RAS for providing necessary facilities to carry out this work.

5. Appendices

5.1. Appendix A. Modulation Functions

The expressions for the ESEEM time profile functions V for the transitions of a triplet spin ($S = 1$) are similar to the expressions found for spin ($S = 1/2$) as discussed in ref. [18]. In an ideal two-pulse experiment, the ESEEM signal induced by the nth nucleus's spin is proportional to the following function [14–18]:

$$V_{ij}(\tau) = 1 - 2k_{ij}\sin^2(\omega_i\tau/2)\sin^2(\omega_j\tau/2). \tag{42}$$

Here, τ is the variable delay between microwave pulses. For a three-pulse ESEEM experiment, the signal is described by the following expression:

$$V(\tau, T) = \big(V_{ij}(\tau, T) + V_{ji}(\tau, T)\big)/2, \tag{43}$$

where

$$V_{ij}(\tau, T) = 1 - 2k_{ij}\sin^2(\omega_j\tau/2)\sin^2\big(\omega_i(\tau+T)/2\big). \tag{44}$$

Here, τ is the fixed delay between the first two microwave pulses, and T is the variable delay between the last two pulses.

The ESEEM signal induced by several nuclei is proportional to the product of the contributions from the individual nuclei. The total signal is expressed as [14–18]:

$$V(\tau) = \prod_n V_n(\tau) \tag{45}$$

in the case of a two-pulse ESEEM sequence, and as:

$$V(\tau, T) = \left(\prod_n V_{n,ij}(\tau, T) + \prod_n V_{n,ji}(\tau, T)\right)/2 \tag{46}$$

in the case of a three-pulse stimulated echo experiment. In equations (45)–(46), the index n labels nearby nuclei while the contributions of the individual nuclei are given by expressions (42)–(44) (without the n index). The mutual influence of the nuclear coherences becomes crucial when the modulation depths of several nuclei are significant ($k \sim 1$). This situation usually occurs for nuclei in near-equivalent conditions (see [33, 34]). However, it is expected that, in organic molecules, unpaired electrons will couple with distant nuclei via dipole-dipole interactions, which depend on the mutual orientation of these species. Therefore, near-equivalent conditions for two or more nuclei are expected to be rare and are beyond the scope of this work.

5.2. Appendix B. Euler Rotation Matrices

The transformation of the spin operators defined in the molecular and laboratory frames can be described by the Euler matrix $\mathbf{R}$:

$$(S_x, S_y, S_z)^{\mathrm{tr}} = \mathbf{R}\cdot(S_X, S_Y, S_Z)^{\mathrm{tr}}. \tag{47}$$

Here, the brackets denote the vector-operator $\mathbf{S}$, which is given by its elements defined in the laboratory ($\xi = x, y, z$) and molecular ($\xi = X, Y, Z$) frames. The term "tr" denotes the transpose operation.

The Euler matrix is set for the zyz convention with the rotation angles φ, θ and ψ as follows:

$$\mathbf{R} = R_z(\varphi)\cdot R_y(\theta)\cdot R_z(\psi) = \begin{pmatrix} \cos\theta\cos\varphi & -\sin\varphi & \sin\theta\cos\varphi \\ \cos\theta\sin\varphi & \cos\varphi & \sin\theta\sin\varphi \\ -\sin\theta & 0 & \cos\theta \end{pmatrix}\cdot\begin{pmatrix} \cos\psi & -\sin\psi & 0 \\ \sin\psi & \cos\psi & 0 \\ 0 & 0 & 1 \end{pmatrix}. \tag{48}$$

For the given definitions, the direction of the external field in the molecular frame is determined as:

$$\mathbf{R}\cdot\mathbf{B}^{\mathrm{tr}} = B\left(\sin\theta\cos\varphi,\ \sin\theta\sin\varphi,\ \cos\theta\right)^{\mathrm{tr}}. \tag{49}$$

The first rotation is around the z-axis, and therefore, the direction of the external field and the spin-Hamiltonian of the triplet state (1) do not depend on the angle ψ. However, this angle is needed to define the other axes as well as the orientation of the nearby nucleus relative to the molecular and laboratory frames. In the laboratory frame, the radius-vector $\mathbf{r} \equiv (r_x, r_y, r_z)$ is determined by the direction cosines. The relationship of this vector to the components (r_X, r_Y, r_Z) of the molecular frame is given by:

$$\mathbf{r} \equiv (r_x, r_y, r_z) = (r_X, r_Y, r_Z)\cdot\mathbf{R}. \tag{50}$$

5.3. Appendix C. Expectation Values

Within the linear approximation of the quantity D/ω_{T}, the eigenvalues of the spin Hamiltonian H_T are equal to the diagonal matrix elements of its matrix given in the laboratory frame:

$$\begin{gathered} E_0 = -2d/3, \\ E_{\pm 1} = \pm\omega_{\mathrm{T}} + d/3, \\ d = -(D/2)\left(1 - 3\cos^2\theta\right) + (3E/2)\sin^2\theta\cos 2\varphi. \end{gathered} \tag{51}$$

The projection operators $P_m = |\psi_m\rangle\langle\psi_m|$ to the eigenstate ψ_m of the Hamiltonian H_T equal [35]:

$$P_m = \prod_{i \neq m} \frac{H_{\mathrm{T}} - \mathbf{1}E_i}{E_m - E_i}. \tag{52}$$

Here **1** is the identity operator. By definition of the projection operators, the expectation value of the spin operator O is given by:

$$\langle O\rangle_m = \mathrm{Tr}(OP_m). \tag{53}$$

The expectation values of the projection operators $S_{m,\xi}$ can be evaluated based on eqs. (51)–(53). Within the linear approximation over the quantity d/ω_{T}, they equal:

$$\begin{gathered} \langle S_x\rangle_0 = 2\big(\chi_1\cos\psi + \chi_2\sin\psi\big), \qquad \langle S_x\rangle_{\pm 1} = -(1/2)\langle S_x\rangle_0, \\ \langle S_y\rangle_0 = 2\big(-\chi_1\sin\psi + \chi_2\cos\psi\big), \qquad \langle S_y\rangle_{\pm 1} = -(1/2)\langle S_y\rangle_0, \\ \langle S_z\rangle_0 = 0, \qquad \langle S_z\rangle_{\pm 1} = \pm 1. \end{gathered} \tag{54}$$

with the auxiliary parameters:

$$\chi_1 = \frac{\big(D - E\cos 2\varphi\big)\sin 2\theta}{2\omega_{\mathrm{T}}}, \quad \chi_2 = \frac{E\sin\theta\sin 2\varphi}{2\omega_{\mathrm{T}}}. \tag{55}$$

Equations (54)–(55) can be used to estimate the influence on ZFS-induced mixing of the triplet spin wave functions on the effective fields (18).

References

1. Teki Y., *Chemistry – A European Journal* **26**, 980 (2020).
2. Gibbons D. J., Farawar A., Mazzella P., Leroy-Lhez S., Williams R. M., *Photochemical & Photobiological Sciences* **19**, 136 (2020).
3. Quintes T., Mayländer M., Richert S., *Nature Reviews Chemistry* **7**, 75 (2023).
4. Bassan E., Gualandi A., Cozzi P. G., Ceroni P., *Chemical Science* **12**, 6607 (2021).
5. Zhang X., Wang Z., Hou Y., Yan Y., Zhao J., Dick B., *Journal of Materials Chemistry C* **9**, 11944 (2021).
6. Wasielewski M. R., Forbes M. D., Frank N. L., Kowalski K., Scholes G. D., Yuen-Zhou J., Baldo M. A., Freedman D. E., Goldsmith R. H., Goodson T., Kirk M. L., McCusker J. K., Ogilvie J. P., Shultz D. A., Stoll S., Whaley B. K., *Nature Reviews Chemistry* **4**, 9 (2020).
7. Santanni F., Privitera A., *Advanced Optical Materials* **12**, 2303036 (2024).
8. Verma N. C., Fessenden R. W., *The Journal of Chemical Physics* **65**, 2139 (1976).

9. Weber S., *eMagRes* **6**, 255 (2017).

10. Filidou V., Mamone S., Simmons S., Karlen S. D., Anderson H. L., Kay C. W. M., Bagno A., Rastrelli F., Murata Y., Komatsu K., Lei X., Li Y., Turro N. J., Levitt M. H., Morton J. J. L., *Philosophical Transactions of the Royal Society A: Mathematical, Physical and Engineering Sciences* **371**, 20120475 (2013).

11. Tait C. E., Neuhaus P., Anderson H. L., Timmel C. R., *Journal of the American Chemical Society* **137**, 6670 (2015).

12. Tait C. E., Neuhaus P., Anderson H. L., Timmel C. R., Carbonera D., Di Valentin M., *Applied Magnetic Resonance* **46**, 389 (2015).

13. Richert S., Tait C. E., Timmel C. R., *Journal of Magnetic Resonance* **280**, 103 (2017), special Issue on Methodological advances in EPR spectroscopy and imaging.

14. Mims W., *Physical Review B* **5**, 2409 (1972).

15. Dikanov S., Shubin A., Parmon V., *Journal of Magnetic Resonance (1969)* **42**, 474 (1981).

16. Stoll S., Calle C., Mitrikas G., Schweiger A., *Journal of Magnetic Resonance* **177**, 93 (2005).

17. Salikhov K. M., Semenov A., Tsvetkov Y., *Electron Spin Echo and Its Application* (Nauka, 1976) [In Russian].

18. Dikanov S. A., Tsvetkov Y., *Electron Spin Echo Envelope Modulation (ESEEM) Spectroscopy* (CRC Press, 1992).

19. Likerov R., Tarasov V., Sukhanov A., Shestakov A., Eremina R., Zavartsev Y., Kutovoi S., *Magnetic Resonance in Solids* **22**, 1 (2020).

20. Borovykh I., Dzuba S., Proskuryakov I., Gast P., Hoff A., *Biochimica et Biophysica Acta (BBA) - Bioenergetics* **1363**, 182 (1998).

21. De Groot A., Evelo R., Hoff A. J., De Beer R., Scheer H., *Chemical Physics Letters* **118**, 48 (1985).

22. Sloop D., Yu H.-L., Lin T.-S., Weissman S., *Journal of Chemical Physics* **75**, 3746 (1981).

23. Yu H.-L., Sloop D., Weissman S., Lin T.-S., Norris J., Bowman M., *The Journal of Physical Chemistry* **86**, 4287 (1982).

24. Lin T.-S., *Chemical Review* **84**, 1 (1982).

25. Di Valentin M., Kay C., Giacometti G., Möbius K., *Chemical Physics Letters* **248**, 434 (1996).

26. Doubinskii A., Lebedev Y., Salikhov K., Möbius K., *Applied Magnetic Resonance* **13**, 459 (1997).

27. Uvarov M., Kulik L., Bizin M., Ivanova V., Zaripov R., Dzuba S., *Magnetic Resonance in Solids* **18**, 15 (2006).

28. Maryasov A. G., Bowman M., Tsvetkov Y., *Applied Magnetic Resonance* **23**, 211 (2002).

29. Kandrashkin Y. E., Zavartsev Y. D., Koutovoi S. A., Sukhanov A. A., *Applied Magnetic Resonance* **49**, 1313 (2018).

30. Weil J. A., Anderson J. H., *The Journal of Chemical Physics* **35**, 1410 (1961).

31. Schweiger A., Jeschke G., *Principles of Pulse Electron Paramagnetic Resonance* (Oxford University Press, 2001).

32. Zalibera M., Krylov D. S., Karagiannis D., Will P.-A., Ziegs F., Schiemenz S., Lubitz W., Reineke S., Savitsky A., Popov A. A., *Angewandte Chemie* **130**, 283 (2018).

33. Kandrashkin Y. E., *Journal of Magnetic Resonance* **365**, 107732 (2024).

34. Kandrashkin Y. E., *Journal of Magnetic Resonance* **365**, 107731 (2024).

35. Maryasov A., Bowman M., Tsvetkov Y., *Applied Magnetic Resonance* **30**, 683 (2006).